crystals

MDPI

Article

Empirical Screening of Two Laser Processing Conditions with Respect to Graphitic Ordering and Electrochemical Performance of PEI-Derived Laser-Induced Carbon

Pamela Rivera Rivera [1], Šarūnas Mickus [2], Aušra Selskienė [3], Tomas Murauskas [3], Sandra Stanionytė [3], Romualdas Trusovas [2], Justina Gaidukevič [1,4] and Rasa Pauliukaite [1,*]

[1] Department of Nanoengineering, Center for Physical Sciences and Technology (FTMC), Savanoriu Ave. 231, LT-02300 Vilnius, Lithuania; pamela.rivera@ftmc.lt (P.R.R.); justina.gaidukevic@ftmc.lt (J.G.)
[2] Department of Laser Technology, Center for Physical Sciences and Technology (FTMC), Savanoriu Ave. 231, LT-02300 Vilnius, Lithuania; sarunas.mickus@ftmc.lt (Š.M.); romualdas.trusovas@ftmc.lt (R.T.)
[3] Department of Characterisation of Materials Structure, Center for Physical Sciences and Technology (FTMC), Sauletekio Ave. 3, LT-02300 Vilnius, Lithuania; ausra.selskiene@ftmc.lt (A.S.); tomas.murauskas@ftmc.lt (T.M.); sandra.stanionyte@ftmc.lt (S.S.)
[4] Faculty of Chemistry and Geosciences, Institute of Chemistry, Vilnius University, Naugarduko Str. 24, LT-03225 Vilnius, Lithuania
* Correspondence: rasa.pauliukaite@ftmc.lt

Abstract

Laser-induced graphene (LIG) enables rapid conversion of polymer substrates into conductive carbon materials. In this study, nitrogen-containing carbon nanomaterials were fabricated on polyetherimide (PEI) substrates using empirical screening of two specific process points. The resulting materials were characterized using scanning electron microscopy, Raman spectroscopy, X-ray photoelectron spectroscopy, cyclic voltammetry, and electrochemical impedance spectroscopy to correlate structural features with electron-transfer behavior. Raman and XPS analyses showed different structure and morphology depending on irradiation regime. The carbon materials with a higher sp^3 fraction (≈55–59%), larger in-plane crystallite size (L_a up to 8.0 nm), and pronounced π–π* shake-up satellites indicated enhanced graphitic ordering when a shorter nanosecond laser was used. These structural differences resulted in substantially lower charge-transfer resistance (0.53–0.79 kΩ·cm^3) and larger electroactive surface areas for the porous electrodes compared with foam structured carbon nanomaterials. The results show that, under the selected fabrication conditions, variations in laser processing parameters correspond to differences in graphitic ordering and electron-transfer properties in PEI-derived laser-induced carbon materials.

Keywords: laser-induced graphene; graphitic ordering; carbon nanomaterials; electrochemical impedance spectroscopy

Academic Editor: John Parthenios

Received: 30 March 2026
Revised: 10 May 2026
Accepted: 12 May 2026
Published: 15 May 2026

1. Introduction

Graphene and other carbon nanomaterials have attracted considerable attention due to their exceptional electrical, mechanical, and chemical properties, enabling applications in energy storage systems, filtration technologies, sensing platforms, and flexible electronics. Conventional graphene synthesis methods, such as chemical vapor deposition (CVD), can yield high-quality materials but typically require extended processing times, hazardous reagents, and costly equipment. Although alternative approaches, such as mechanical milling or physical exfoliation of graphite, are more economical, the structural quality

and electronic performance of the resulting materials are often inferior compared to those obtained via more sophisticated techniques [1]. Consequently, the development of rapid, scalable, and cost-effective strategies for producing conductive carbon nanomaterials remains an important research priority.

Laser-induced graphene (LIG) has emerged as a promising alternative due to its simplicity, low cost, and rapid fabrication process [2]. Laser irradiation enables the direct conversion of insulating polymers, such as polyimide (PI) or polyetherimide (PEI), into porous, graphene-like conductive networks through localized photothermal carbonization. The resulting materials typically exhibit a three-dimensional architecture with tunable defect density, heteroatom content, and surface morphology, making them particularly attractive for electrochemical applications.

The structural and functional properties of LIG are strongly governed by the laser–material interaction regime, which depends on multiple irradiation parameters, including wavelength, pulse duration, energy density, and thermal dynamics [3–6]. While CO_2 infrared lasers (10.6 μm) are widely employed due to their efficient photothermal conversion and accessibility, visible nanosecond lasers (e.g., 532 nm) interact with polymer substrates through distinct absorption characteristics and energy deposition profiles. Although numerous studies report the fabrication and application of LIG electrodes, systematic investigations that directly correlate specific irradiation regimes with graphitic ordering and quantitative interfacial charge-transfer kinetics remain limited. In particular, comparative studies that combine structural characterization (Raman and XPS) with rigorous electrochemical impedance modeling to elucidate transport-dominated performance differences are scarce.

For electrochemical applications, performance is governed not only by surface area and defect density but also by electronic transport properties, graphitic domain size, and the quality of the electrode–electrolyte interface [7,8]. Raman spectroscopy and X-ray photoelectron spectroscopy (XPS) provide insights into structural ordering and surface chemistry [9–11], while electrochemical impedance spectroscopy (EIS) enables quantitative assessment of charge-transfer resistance and interfacial capacitance [12,13]. However, the relative contributions of graphitic ordering versus heteroatom functionalization to charge-transfer efficiency in LIG systems are still insufficiently clarified.

This work is a proof-of-concept study aimed at identifying key differences of graphitization of polyetherimide (PEI) employing two specific process points. Nitrogen-doped carbon nanomaterials were fabricated directly on PEI substrates using a CO_2 laser and a nanosecond green laser. The resulting materials were comprehensively characterized by scanning electron microscopy (SEM), Raman spectroscopy, XPS, cyclic voltammetry (CV), and EIS to correlate structural features with interfacial charge-transfer behavior. Accordingly, this comparison should be interpreted as an empirical evaluation under defined irradiation conditions, in which multiple processing parameters contribute to the observed outcomes. By relating structural metrics to electrochemical behavior, this study reports trends associated with variations in graphitic character and electron-transfer kinetics in laser-induced carbon electrodes.

2. Materials and Methods

2.1. Materials

Commercial PEI sheets (Ultem® 1000, unfilled grade) (PrimaCreator, Malmö, Sweden) were used as the precursor substrate. Sodium acetate, nitric acid (≥69%), cadmium nitrate tetrahydrate ($Cd(NO_3)_2 \cdot 4H_2O$), lead(II) nitrate ($Pb(NO_3)_2$), and glacial acetic acid (≥99.7%) were purchased from Sigma-Aldrich (St. Louis, MO, USA). Zinc nitrate hexahy-

drate ($Zn(NO_3)_2 \cdot 6H_2O$, ≥96% purity) was obtained from Carl Roth (Karlsruhe, Germany). Ultrapure water (18.2 MΩ·cm) was used for the preparation of all solutions.

2.2. Methods

2.2.1. Scanning Electron Microscopy

An Helios Nanolab 650 scanning electron microscope (SEM) (FEI, Eindhoven, The Netherlands) equipped with an energy-dispersive X-ray spectrometer (Oxford Instruments, Abingdon, UK, Xmax 20 mm^2 detector, INCA 4.15 software) was used for sample surface investigation. The samples were examined in the secondary electron imaging (SEI) mode at 3 kV acceleration voltage and 25 pA beam current. The elemental analysis was performed using 5 kV acceleration voltage and 1.6 nA beam current.

2.2.2. X-Ray Photoelectron Spectroscopy

X-ray photoelectron spectroscopy (XPS) measurements were performed using a Kratos Axis Supra spectrometer (Kratos Analytical, Kyoto, Japan) equipped with a monochromatic Al Kα radiation source (1486.69 eV). Spectral calibration was carried out based on the C 1 s peak set at 284.6 eV, and data were collected using a pass energy of 20 eV. The collected spectra were processed and deconvoluted using CasaXPS software Version 2.3.25PR1.0. After subtracting a Shirley-type background, the peaks were fitted with symmetric Gaussian–Lorentzian functions.

2.2.3. Raman Spectroscopy

Raman measurements were performed with a Raman spectrometer/microscope in Via (Renishaw, Wotton-under-Edge, UK) equipped with a thermoelectrically cooled (−70 °C) CCD detector. Spectra were excited with the 532 nm wavelength laser and dispersed by 1800 grooves/mm grating. Raman spectra were taken using a 50×/0.75 NA objective lens. The raw Raman data were processed using Origin 2021 Pro software. The structural metrics were quantified by performing a spectral deconvolution using a Lorentzian function to resolve the primary vibrational modes of the samples.

To mitigate the interference from the PEI substrate, a laser preirradiation (photobleaching) procedure was implemented. Specifically, the measurement spot was exposed to the 532 nm laser for 500 s prior to spectral acquisition. Following this treatment, Raman spectra were collected from the same location using identical measurement conditions (100 s acquisition). This approach effectively reduced background interference and enabled clear observation of the characteristic D, G, and 2D bands in the PEI spectra.

2.2.4. Cyclic Voltammetry

Cyclic voltammetry (CV) measurements were performed with PalmSens4 potentiostat (PalmSens, Houten, The Netherlands) in a 0.1 M KCl/HCl solution (pH 2.0) containing 10.0 mM $K_4[Fe(CN)_6]$ using a three-electrode configuration with the LINDCN sample as the working electrode, Ag/AgCl (3 M KCl) as the reference electrode, and a platinum wire as the counter electrode. The potential was cycled within the range of 1.0 V to −1.0 V, using a potential step of 7 mV. CVs were recorded at different potential scan rates to evaluate the electron-transfer characteristics of the LINDCN electrodes. The geometric area of the electrode exposed to the electrochemical reaction was 1 cm^3.

2.2.5. Electrochemical Impedance Spectroscopy

EIS measurements were performed using an IviumStat (Ivium Technologies, Eindhoven, The Netherlands) or PalmSens4 potentiostats in a three-electrode configuration identical to that used for CV, with LINDCN as the working electrode (geometric area 1 cm^3), Ag/AgCl (3 M KCl) as the reference electrode, and a platinum wire as the counter electrode.

EIS measurements in blank electrolyte were carried out in 1.0 M KCl. Prior to each measurement, the electrode was allowed to equilibrate for 10 s at the applied potential. Spectra were recorded by applying a 5 mV sinusoidal AC perturbation superimposed on a 0.00 V DC bias over a frequency range from 100 kHz to 0.1 Hz, using 31 logarithmically spaced frequency points.

To evaluate interfacial charge-transfer behavior, EIS was additionally performed in the presence of a redox probe − 5.0 mM $[Fe(CN)_6]^{3-}/^{4-}$ in 0.1 M KCl. Measurements were conducted at open-circuit potential following a 30 s equilibration period, using a 5 mV AC amplitude over the same frequency range (100 kHz to 0.1 Hz), with 61 frequency points (10 per decade). The spectra were analyzed using either ZView2 or PSTrace4 software, depending on which instrument was used to register spectra.

2.2.6. Square Wave Adsorptive Stripping Voltammetry

Square wave adsorptive stripping voltammetry (SWASV) was conducted using the IviumStat potentiostat in the same three-electrode electrochemical cell. Adsorption was performed at the potential of 1.4 V vs. Ag/AgCl for 5 min. The SWASV parameters were set as follows: frequency of 20 Hz, amplitude of 40 mV, and step potential of 5 mV.

2.3. Synthesis of Laser-Induced N-Doped Carbon Nanomaterials

Laser-induced carbon nanomaterials were fabricated on PEI sheets (0.5 mm thickness) using two laser systems: a CO_2 laser (10.6 μm) and a nanosecond 532 nm laser (Lithuania). For the CO_2 laser, patterning was performed under ambient atmosphere using 1.4 W power, 18 mm s^{-1} scan speed, 0.05 mm hatch spacing, and two passes, with the beam focused using a 250 mm focal length lens. For the 532 nm laser, a 10 ns pulsed laser operating at 100 kHz was used with 300 mW power, scan speeds of 70 or 100 mm s^{-1}, 0.02 mm hatch spacing, and three passes, with a 4 mm positive defocus using a 100 mm focal length lens. Two samples were fabricated under both laser irradiation conditions and designated LINDCN_CO_2-1, LINDCN_CO_2-2, LINDCN_532-1, and LINDCN_532-2.

3. Results

As stated in the Introduction, LIG materials are usually produced using a CO_2 pulsed laser on the PI surface [14]. To compare the quality of the obtained laser-induced nitrogen-doped carbon nanomaterials (LINDCNs), those under both laser irradiation conditions were also used with PEI. The obtained LINDCNs were characterized using SEM, XPS, and Raman spectroscopy, commonly used to evaluate the quality of carbon nanomaterials. Electrochemical methods were also used to assess the suitability of LINDCN as a platform for electrochemical sensing.

3.1. LINDCN Characterization

3.1.1. Surface Morphology

SEM images were recorded in order to evaluate the surface morphology of the obtained LINDCNs. Zooms of 150×, 1000×, 10,000×, and 50,000× were used for characterization. The surface morphologies of LINDCN_CO_2-1 and LINDCN_CO_2-2 were similar, with both exhibiting clear lines caused by the laser beam, as well as large, porous structures formed by the photothermal and photochemical processes of PEI resulting from laser irradiation (Figure 1A–D) as observed on the PI surface [2,15]. These structures were visible on both LINDCN sample surfaces, with a pore size of 5–50 μm. This structure is formed by PEI swelling and blistering during the photothermal process as obtained for PI [15]. Abdulhafez et al. also observed a clearly defined porous structure with isotropic pores on a polyimide surface. The authors clarified that such structures are obtained using a

focused beam with a fluence of z = 3.6 mm. The fact that both samples have the same structure indicates that the morphology of LINDCN on a PEI surface can be reproduced using identical laser parameters. Increasing the magnification, LINDCN_CO_2 samples revealed some kind of nanoparticle on the surface (Figure 1B,D), showing that the obtained material is carbon nanostructures rather than graphitic materials. Wal et al. obtained a similar surface morphology on PI [16], but they used microwave-driven plasma-mediated methane cracking to produce carbon.

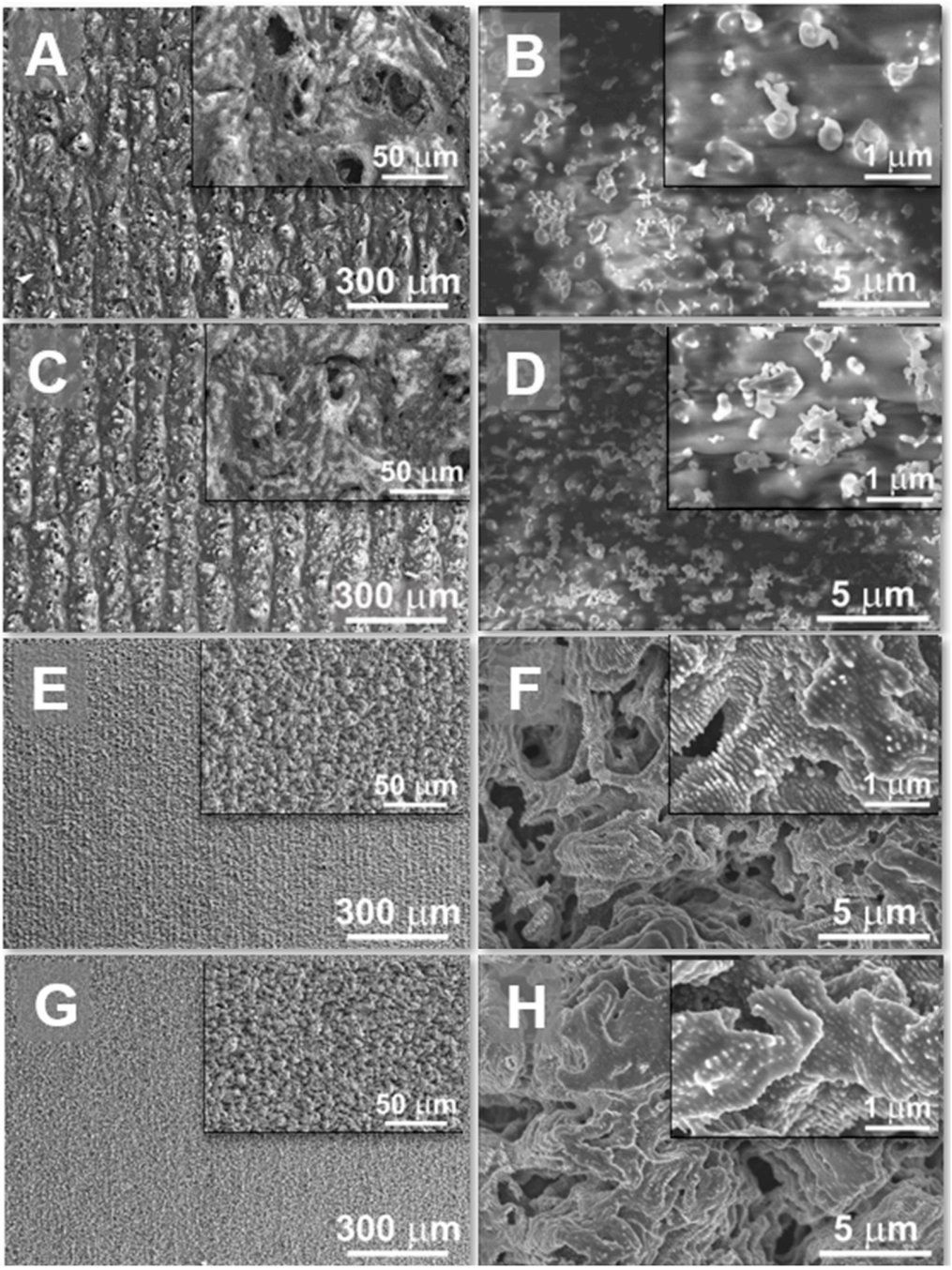

Figure 1. SEM images of LINDCN_CO_2-1 (**A**,**B**), LINDCN_CO_2-2 (**C**,**D**), LINDCN_532-1 (**E**,**F**), and LINDCN_532-2 (**G**,**H**) at different magnifications.

The morphology of the LINDC_532 appeared different (Figure 1E–H). Lines from the laser irradiation are also visible on the surface of these samples, but they are less expressed than in the case of LINDCN_CO_2 (Figure 1E,G). Furthermore, the structures

are also smaller than those on the LINDCN_CO_2 samples. Moreover, the pores were also significantly smaller, i.e., 1–5 μm, clearly visible at high magnifications (Figure 1F,H).

It is important to note that the morphology differences are caused by different mechanisms of action of each of these lasers. CO_2 and 532 nm nanosecond lasers operate under fundamentally different energy–matter interaction regimes. For CO_2 laser irradiation ($\lambda \approx 10.6$ μm), the interaction is dominated by vibrational absorption within the polymer matrix, which leads to efficient conversion of laser energy into heat over a relatively large interaction volume. This produces a photothermal regime in which temperatures exceed 2000 K, driving the reorganization of carbon atoms into sp^3-bonded networks. The prolonged thermal exposure promotes graphitization and substantial gas evolution (e.g., CO, CO_2), resulting in the characteristic three-dimensional porous morphology of LIG. In this case, graphene formation is primarily governed by thermally driven carbonization pathways that approach local thermodynamic equilibrium. This mechanism has been widely reported for CO_2-laser-induced graphene on polymers such as polyimide and lignin-based precursors and others [17].

In contrast, irradiation with a 532 nm nanosecond laser introduces a fundamentally different interaction mechanism. Due to the shorter wavelength and higher photon energy, absorption is more strongly associated with electronic excitation rather than purely vibrational modes, and energy deposition occurs over much shorter timescales [18]. As a result, the process is inherently non-equilibrium, involving a combination of localized photothermal heating, photochemical bond disruption, and, at higher fluences, photomechanical effects such as ablation or exfoliation. Such mechanisms, including laser-induced exfoliation and non-thermal bond breaking, have been reported in studies of visible- and near-IR-pulsed-laser processing of carbon precursors and graphene oxide [19,20].

This distinction in energy coupling—bulk thermal heating versus localized electronic excitation—directly influences the carbonization pathway and ultimately the resulting material properties. While CO_2 laser processing favors porous, foam-like graphene structures with a large surface area, the 532 nm nanosecond laser tends to produce denser, more planar or layered carbon structures, reflecting the reduced role of sustained high-temperature pyrolysis and the increased contribution of non-thermal mechanisms [21–23].

3.1.2. Chemical and Structural Composition

EDS and XPS analyses were performed to confirm the elemental composition of the LINDCN samples. EDS was performed in conjunction with SEM morphology studies. The EDS and XPS analysis data are shown in Table 1. As expected, carbon was the most abundant element, accounting for approximately 84% and 98% of LINDCN_CO_2 and LINDCN_532, respectively. Oxygen accounted for approximately 11% of LINDCN_CO_2 and 1.8% of LINDCN_532. Around 5% of LINDCN_CO_2 was nitrogen, indicating that PEI was not fully carbonized. Nevertheless, nitrogen was below the detection limit (which is 0.1%) in the LINDCN_532 samples. Here and below, all data are given in atomic %. The XPS results revealed a noticeably different surface composition. For LINDCN_CO_2, the average surface composition was 76.64 at.% C, 4.58 at.% N, and 18.78 at.% O, while for LINDCN_532 it was 83.12 at.% C, 3.28 at.% N, and 13.59 at.% O. Importantly, unlike EDS, XPS also detected nitrogen on the surface of the LINDCN_532 samples, indicating that N-containing species were still present, although in amounts too low to be detected by EDS. The discrepancy between EDS and XPS most likely arises from the different information depths and sensitivities of the two techniques. XPS is a highly surface-sensitive method, typically probing the outermost <10 nm of the material, whereas SEM-EDS provides bulk-averaged information with an interaction depth of approximately 0.3–3.0 μm [24,25]. In addition, EDS quantification of light elements such as nitrogen is less reliable, especially for

rough, porous, or heterogeneous carbon-based materials. Furthermore, XPS consistently showed lower carbon and higher oxygen contents than EDS for both sample series, indicating that oxygen-containing functional groups are predominantly located on the surface rather than in the bulk of the material.

Table 1. Elemental composition (atomic %) of the samples as determined by XPS and EDS.

Sample	EDS				XPS			
	C	N	O	C/O	C	N	O	C/O
LINDCN_CO_2-1	84.04	5.00	10.96	7.67	78.98	4.56	16.46	4.80
LINDCN_CO_2-2	84.17	4.79	11.04	7.62	74.30	4.59	21.10	3.52
Average	84.11	4.89	11.00	7.65	76.64	4.58	18.78	4.16
LINDCN_532-1	98.22	<0.1	1.79	55.02	83.96	3.31	12.70	6.61
LINDCN_532-2	98.30	<0.1	1.70	57.82	82.27	3.25	14.48	5.68
Average	98.26	<0.1	1.74	56.42	83.12	3.28	13.59	6.15

Wu et al. [17] stated that the underlying LIG formation chemical mechanism also depends on the precursor material. Although in the majority of studies LIG is formed on poly(4,4′-oxydiphenylene-pyromellitimide) (PI), which contains nitrogen atoms in its backbone, 2,2-bis(4-(2,3-dicarboxyphenoxy)phenyl)propane dianhydride (PEI; Figure 2) also contains nitrogen in phthalimide groups and is likewise suitable as a precursor for LIG, with a similar formation mechanism. The process most likely involves photochemical bond disruption via oxidation of the bisphenol moiety [26], which can subsequently contribute either to graphitization or to the formation of oxygen-containing functional groups. The observed similarity in surface morphology between PI [15,16] and PEI (in our case) supports the hypothesis that the underlying graphitization mechanism is likely similar.

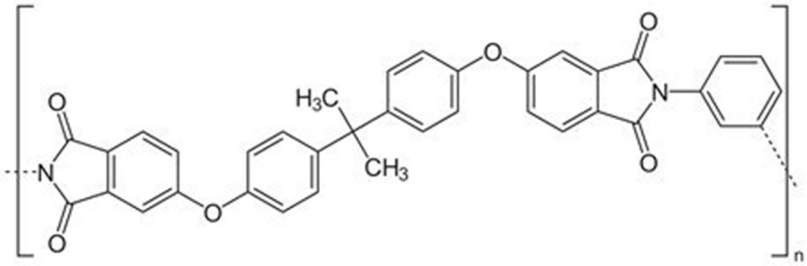

Figure 2. PEI chemical structure.

According to the literature, the C/O ratio is an important parameter that indicates the conductivity and structural properties of LIG [27]. In both sample types, the C/O ratio was high (7.65 for LINDCN_CO_2 and 56.4 for LINDCN_532), indicating a reduced graphene structure and improved conductivity. However, LINDCN_532 exhibited the highest C/O ratio (ca. 7.4 times higher than LINDCN_CO_2). Similar results were obtained when comparing CO_2 and UV laser irradiations: the LIG produced on PI using the UV laser had a slightly higher C/O ratio (17.3) than that produced using the CO_2 laser (11.0) [28]. These results differ considerably from those reported in [19], where the authors doped the LIG with phosphorus during fabrication. The C/O ratio was just 0.588, and the LIG contained 18.92% phosphorus (P). Moreover, different laser parameters were used. A significantly lower C/O ratio (ranging from 3 to 27, depending on laser pulse duration and irradiation dose) was also found when LIG was prepared from pinewood [27].

As can be seen in Table 1, the composition of the samples obtained using the same laser was reproducible.

The chemical composition and bonding configuration of the LINDCN samples were examined using XPS, and the high-resolution C1s spectra are presented in Figure 3a.

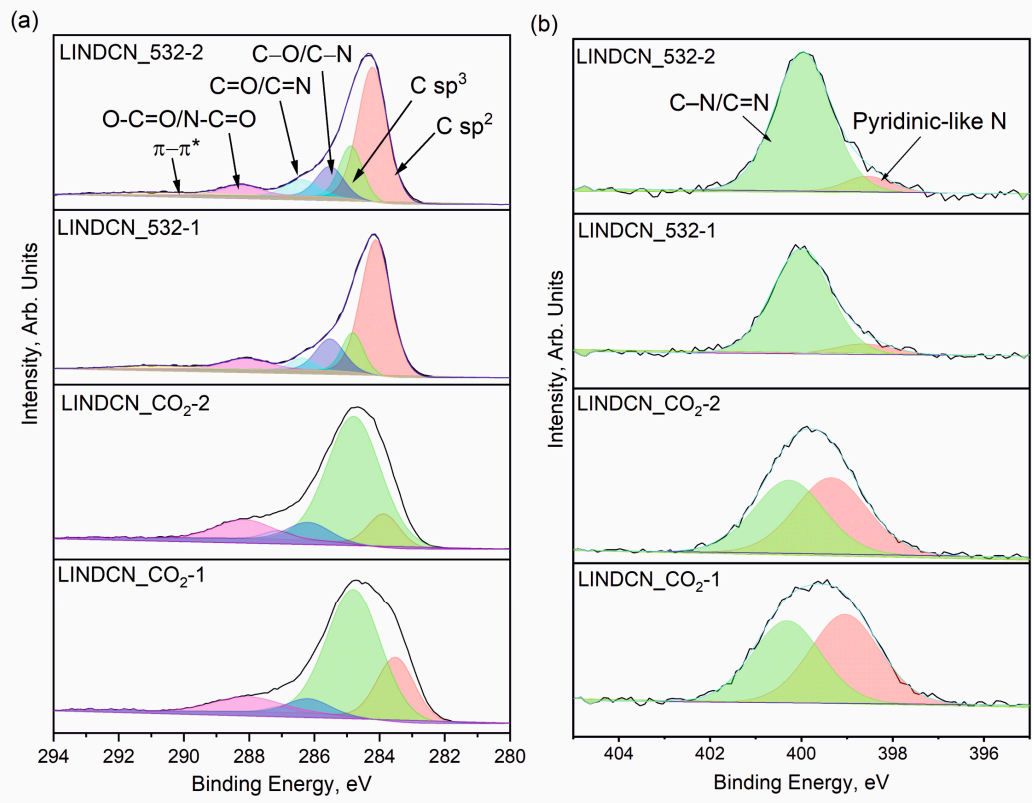

Figure 3. High-resolution XPS C1s (**a**) and N1s (**b**) spectra of LINDCN samples prepared using CO_2 and 532 nm lasers. Fitting components of C1s: C sp^2 (pink), C sp^3 (green), C–O/C–N (violet), C=O/C=N (blue), O–C=O/N–C=O (magenta), and π–π* (grey) (**a**); N1s: C–N/C=N (green) and pyridinic-like N (pink).

The C1s spectra of the CO_2-laser-treated samples (LINDCN_CO_2-1 and LINDCN_CO_2-2) were deconvoluted into five components centered at approximately 283.5–283.9 eV (sp^2 C=C), 284.8 eV (sp^3 C–C), 286.2 eV (C–O/C–N), 287.1 eV (C=O/C=N), and 288.1 eV (O–C=O/N–C=O) [29–31]. In addition, a π–π* shake-up satellite at ~290.9 eV was observed only for the LINDCN samples, indicating the presence of extended aromatic sp^2 domains [32]. The data are in good agreement with the morphology data obtained with SEM, showing a carbon nanostructured surface (Figure 1A–D).

The presence of oxygen- and nitrogen-containing functional groups, including hydroxyl, epoxy, or amine-type (C–O/C–N, 5.39%), carbonyl or imine (C=O/C=N, 1.25%), and carboxyl or amide-type (O–C=O/N–C=O, 8.80%) species, confirms substantial surface functionalization of the carbon network (Table 2). A comparable composition was observed for LINDCN_CO_2-2, which exhibits an even lower sp^2 carbon content (10.82%) and a higher sp^3 contribution (69.01%), indicating a less aromatic and more amorphous structure. The relative abundance of oxygen-containing groups was also comparable, including C–O/C–N (7.36%), C=O/C=N (2.34%), and O–C=O/N–C=O (10.47%). The absence of a detectable π–π* shake-up satellite in both CO_2-treated samples supports their limited extent of extended aromatic conjugation. Minor differences between the LINDCN_CO_2 samples indicate some variability in laser-induced structural modifications.

Table 2. Analysis of the XPS spectra for LINDCN samples from C1s and N1s spectra in Figure 3.

Sample	Binding Energy, eV (Relative Area, %)							
	C1s						N1s	
	C sp^2	C sp^3	C–O/C–N	C=O/ C=N	O–C=O/ N–C=O	π–π*	C–N/ C=N	Pyridinic-Like N
LINDCN_CO_2-1	283.5 (22.08)	284.8 (62.48)	286.2 (5.39)	287.1 (1.25)	288.1 (8.8)	-	400.3 (47.62)	399.0 (52.38)
LINDCN_CO_2-2	283.9 (10.82)	284.8 (69.01)	286.2 (7.36)	287.1 (2.34)	288.1 (10.47)	-	400.3 (48.47)	399.3 (51.53)
LINDCN_532-1	284.1 (59.48)	284.8 (12.52)	285.5 (13.21)	286.4 (4.04)	288.1 (7.32)	290.9 (3.43)	400.0 (90.84)	398.6 (9.16)
LINDCN_532-2	284.2 (54.67)	284.8 (17.10)	285.5 (11.51)	286.4 (7.31)	288.2 (5.57)	290.9 (3.84)	400.0 (91.56)	398.6 (8.44)

In contrast, the LINDCN_532 samples exhibit a more consistent chemical composition. Both samples are dominated by sp^2-hybridized carbon, with contributions of 59.48% and 54.67%, respectively, indicative of a well-developed graphitic framework. The data are in good agreement with the surface morphology, indicating graphitic structure (Figure 1E–H, Table 2). The significantly lower sp^3 C–C content compared to the CO_2-treated samples reflects reduced structural disorder. Although oxygen- and nitrogen-containing functional groups are still present, the pronounced π–π* shake-up satellite peaks at ~290.9 eV and the higher sp^2 fraction confirm the formation of extended aromatic domains characteristic of graphitic carbon [31,32]. The presence of C–O/C–N (13.21% for LINDCN_532-1 and 11.51% for LINDCN_532-2), C=O/C=N (4.04% for LINDCN_532-1 and 7.31% for LINDCN_532-2), and O–C=O/N–C=O (7.32% for LINDCN_532-1 and 5.57% for LINDCN_532-2) indicates that a moderate level of surface functionalization is retained after laser processing.

Defect-dominated carbon frameworks with a high density of surface functional groups are advantageous for applications requiring abundant active sites, such as electrochemical sensing in LINDCN_CO_2 samples. In contrast, LINDCNG_532 had a higher proportion of sp^2 carbon, pronounced π–π* interactions, and a more ordered aromatic framework, which is expected to provide enhanced electrical conductivity [33].

Analysis of the N1s spectra of the laser-treated PEI samples revealed two main components centered at approximately 399.0 eV and 400.0 eV. The higher binding energy feature (~400.0–400.3 eV) is attributed to amine-type nitrogen (C–N/C=N), originating from the polyethyleneimine structure and its laser-induced chemical modifications [34]. The formation of imine groups is associated with laser-driven dehydrogenation and crosslinking of amine functionalities, which represents the dominant chemical transformation of PEI under localized thermal conditions [35].

The lower binding energy component (~398.6–399.3 eV) is assigned to pyridinic-like nitrogen [31]. Taken together, the relative intensities of these components demonstrate that laser processing induces substantial chemical restructuring of PEI, resulting in a coexistence of residual amine/imine nitrogen and newly formed pyridinic-like nitrogen. The dominance of amine/imine nitrogen in LINDCN_532 samples arises from localized dehydrogenation and crosslinking of PEI, whereas the increased contribution of pyridinic-like nitrogen in the LINDCN_CO_2 samples reflects deeper laser-induced carbonization and incorporation of nitrogen into conjugated carbon structures.

Further structural analysis was performed using resonance Raman spectroscopy, which is the main tool for the evaluation of the quality of graphitic nanomaterials [36–38].

The Raman spectra obtained for the LINDCN samples, shown in Figure 4, exhibit features typical of graphene-based materials. The spectra are dominated by two first-order bands, namely the D and G bands, located at approximately 1365 and 1583 cm^{-1}, respectively. The G band originates from in-plane vibrational modes of sp^2-hybridized carbon atoms that are part of aromatic rings and conjugated chains (E2g phonon mode). In contrast, the D band originates from breathing-type vibrations of six-membered sp^2 carbon rings (A1g mode) and becomes Raman-active only in the presence of structural defects or lattice disorder, reflecting the breaking of translational symmetry in the sp^2 carbon network [39].

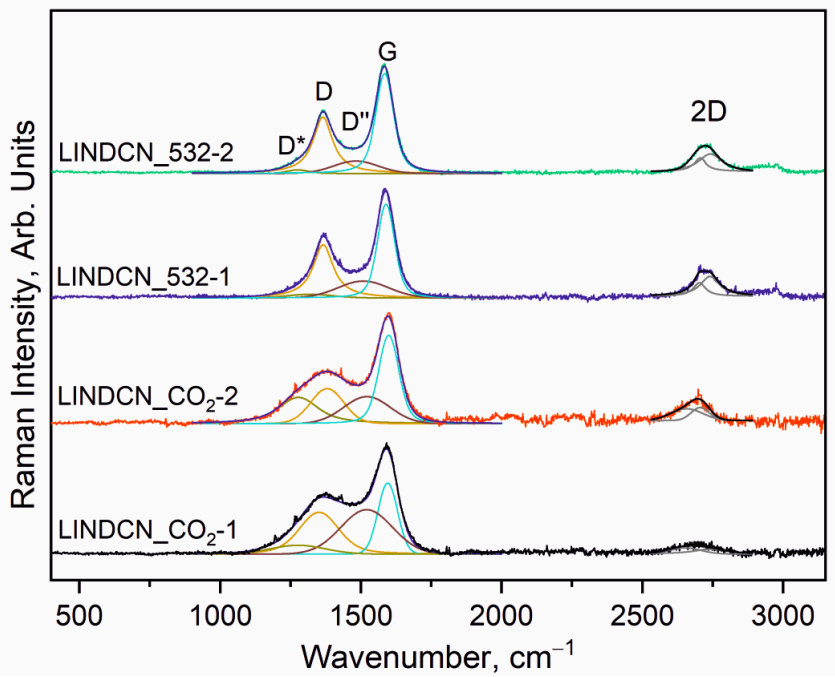

Figure 4. Raman spectra of LINDCN samples with fitted Lorentzian–Gaussian (D (yellow line), G (blue line), 2D (black line), D″ (maroon line) and D* (dark yellow line) bands).

In addition to these first-order features, the presence of the 2D band is related to the stacking and interaction of graphene layers along the c-axis [40]. Furthermore, in more oxidized or highly disordered graphene-derived materials, additional broad features such as the D* band in the 1100–1250 cm^{-1} region and the D′′ band around 1500–1550 cm^{-1} are observed and are commonly associated with sp^3-hybridized carbon species and amorphous carbon phases, respectively [41–43]. Notably, both of these features are also present in the LINDCN samples.

Another key quantitative parameter related to the structure of graphitic nanomaterials can be obtained by analyzing the full width at half maximum of the G band (FWHM(G)) [38]. The determined FWHM(G) value can likewise be employed to estimate the parameter L_a [27]:

$$L_a = \frac{l_c}{2} \ln\left(\frac{c}{\mathrm{FWHM(G)} - \mathrm{FWHM(G_0)}}\right) \quad (1)$$

where *lc* is the photon coherence length (32 nm), C = 95 cm^{-1}, and FWHM(G_0) is the width of the G band of undoped pristine graphene (15 cm^{-1}). Equation (1) is valid for L_a between 2.8 and 32 nm [44]. Moreover, it can also be related to the fact that the D band for LINDCN_CO_2 samples was not sharp. The corresponding G band parameters and calculated L_a values are summarized in Table 3.

Table 3. Analysis of the Raman spectra for LINDCN samples.

LINDCN	I_D/I_G	FWHM(G), cm^{-1}	FWHM(2D), cm^{-1}	L_a, nm	$I_{D''}/I_G$
LINDCN_CO_2-1	0.74	88.7	144.0	4.1	0.40
LINDCN_CO_2-2	0.60	83.7	117.1	5.2	0.24
LINDCN_532-1	0.56	72.5	98.4	8.0	0.15
LINDCN_532-2	0.56	78.0	108.4	6.6	0.10

As summarized in Table 3, the Raman parameters of the LINDCN samples strongly depend on the laser type used during synthesis. Overall, all LINDCN samples exhibit relatively large FWHM(G) values, ranging from 72.5 to 88.7 cm^{-1}. The pronounced broadening of the G band, together with the higher I_D/I_G ratios, consistently reflects a high density of defects in the sp^2 carbon network, resulting from rapid localized heating during laser irradiation [45,46]. The samples produced using the CO_2 laser show the largest FWHM(G) values (88.7 cm^{-1} for LINDCN_CO_2-1 and 83.7 cm^{-1} for LINDCN_CO_2-2), indicating moderate to high disorder in the crystallinity and a relatively large number of defects associated with the presence of functional groups [40,47], which is in good agreement with the XPS data. In contrast, the LINDCN_532-1 and LINDCN_532-2 samples exhibit lower FWHM(G) values (72.5 and 78.0 cm^{-1}, respectively), suggesting a slightly higher structural order and more efficient graphitization. This difference can be attributed to the different laser–material interaction mechanisms associated with different laser parameters [17–20] (see Section 3.1.1).

The calculated in-plane crystallite size (L_a) values range from 4.1 to 8.0 nm, confirming the presence of small graphitic domains in all LINDCN samples. The smallest L_a value is observed for LINDCN_CO_2-1 (4.1 nm), while the largest crystallite size is obtained for LINDCN_532-1 (8.0 nm). Larger L_a values are indicative of more extended sp^2 domains with fewer structural interruptions, suggesting again that irradiation with a 532 nm laser promotes more efficient graphitization compared to CO_2 laser processing.

The $I_{D''}/I_G$ intensity ratio was used to evaluate the degree of amorphization in the LINDCN samples. The LINDCN_CO_2 samples exhibit higher $I_{D''}/I_G$ values (0.40 and 0.24) compared to the LINDCN_532 samples (0.15 and 0.10), indicating a higher contribution of amorphous carbon and greater structural disorder in the LINDCN_CO_2 samples.

The full width at half maximum of the 2D band (FWHM(2D)) values are widely employed to assess both the layer count and the stacking arrangement in graphene-like materials [48]. It has been reported that single-layer graphene typically exhibits a narrow 2D band with an FWHM(2D) of approximately 30 cm^{-1}, while an increase in the number of stacked graphene layers leads to a progressive broadening of this band [49]. In addition, the shape and width of the 2D band allow differentiation between few-layer and multilayer graphene structures. In monolayer graphene, the 2D band consists of a single component, in bilayer graphene, it can be decomposed into four components, and in multilayer graphene, the 2D band can be separated into two components. The measured FWHM(2D) values for the synthesized samples (Figure 4) are greater than 30 cm^{-1} and are most accurately described using a two-component fit, suggesting that the materials produced in this study possess a multilayer structure.

All structural and morphological methods showed inhomogeneity of LINDCN obtained on the PEI surface. According to the literature, the best LIG for biosensing applications is when the structure is highly disordered, i.e., the I_D/I_G ratio is ca. 0.9 [50] to 3.5 [49] and, with multilayered structures, the I_{2D}/I_G ratio is between 0.35 [51] and 0.44 [50]. Both LINDCNs indicated a moderate applicability to electrochemical sensing.

3.1.3. Electrochemical Characterization

The electrochemical characterization of different LINDCN electrodes was performed using CV with the usual redox probe $K_4[Fe(CN)_6]$ to assess the process-limiting step and electron-transfer kinetics. The profile of the CVs depended significantly on the laser used for LINDCN fabrication. Current density and quasi-reversible behavior for LINDCN_CO_2 (Figure 5A,B) were substantially lower than those obtained for LINDCN_532 (Figure 5C,D). It was also noted that LINDCN_CO_2, with the set of parameters described in the Materials and Methods, exhibited inconsistent electrochemical properties, as also revealed by Raman spectroscopy, which showed different I_D/I_G and I_{2D}/I_G values (Figure 4) and XPS data (Figure 3). These results indicate that further optimization of other CO_2 laser parameters is required to obtain LINDCN suitable for electrochemical sensing.

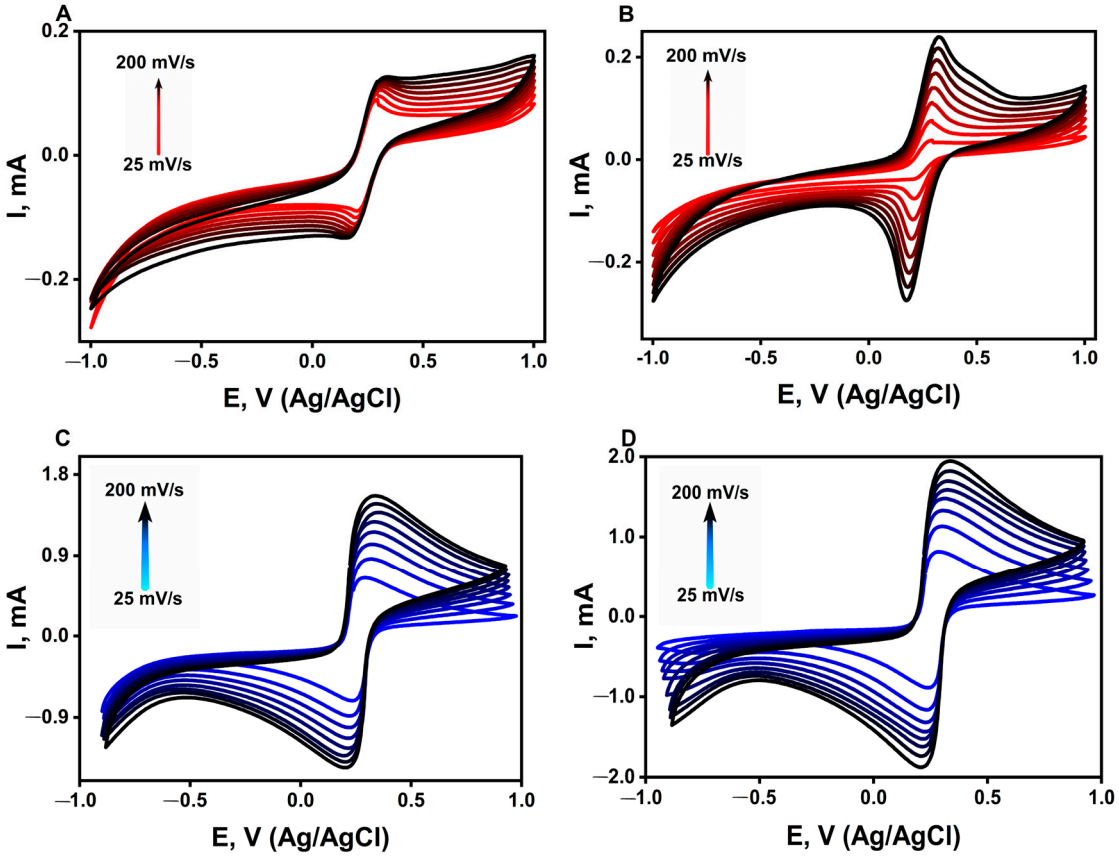

Figure 5. CVs recorded at LINDCD_CO_2-1 (**A**), LINDCD_CO_2-2 (**B**), LINDCD_532-1 (**C**), LINDCD_532-2 (**D**) at different scan rates in 0.1 M KCl solution containing 10 mM $K_4[Fe(CN)_6]$.

To evaluate the electrochemical behavior of the LINDCN electrodes, CVs were recorded at different potential scan rates to determine the limiting step of the electrochemical reaction (Figure 5). All electrodes had a linear relationship of the current density on the square root of the potential scan rate (insets in Figure 4), usually indicating a diffusion-controlled process [52]. However, in the case of the LINDCN_CO_2-1 electrode (Figure 5A), the slopes for oxidation and reduction were low, i.e., 23.6 and –27.4 μA cm^{-2} $V^{1/2}$ $s^{-1/2}$ (inset of Figure 5A), which could be due to adsorption as a limiting step or slow kinetics [52]. In this case, slow kinetics are more likely than an adsorption-controlled process because no other indications were obtained to confirm slow adsorption. Moreover, the LINDCN_CO_2-2 electrode exhibited clear diffusion-controlled behavior (inset of Figure 5B) with the slopes of 118.2 and −166.2 μA cm^{-2} $V^{1/2}$ $s^{-1/2}$.

Both LINDCN_CO_2 electrodes exhibited quasi-reversible electron-transfer behavior (Figure 5A,B). For LINDCN_CO_2-1, the peak-to-peak separation was 88 mV at a scan rate of 25 mV s^{-1} and increased with higher scan rates, while the peak current ratio (I_{ox}/I_{red}) was 1.10. Similarly, LINDCN_CO_2-2 showed a peak-to-peak separation of 86 mV at 25 mV s^{-1}, with an I_{ox}/I_{red} ratio of 0.900. These values indicate that the Randles–Ševčík equation, typically applied to reversible systems, could not provide an accurate determination of the electroactive surface area in this case. Applied *IR* compensation, using cell resistance obtained from analysis of EIS spectra, did not change the peak-to-peak separation significantly (85 and 78 mV for LINDCN_CO_2-1 and LINDCN_CO_2-2, respectively, at 25 mV s^{-1}). Masood et al. [53] precisely and elegantly explained and discussed the most accurate modification of the Randles–Ševčík equation. Consequently, the modified Randles–Ševčík equation was employed for this purpose [53]:

$$I_p = 2.99 \times 10^5 ACn(\alpha n D v)^{1/2} \quad (2)$$

where I_p is the peak current in [A], A is the surface area of the working electrode in [cm^2], c is the concentration of the redox compound (in this case $[Fe(CN)_6]^{4-}$) in [mmol cm^{-3}], n is the number of electrons participating in the electrochemical reaction, α is the transfer coefficient, D is the diffusion coefficient of the redox species ($[Fe(CN)_6]^{4-}$) in [cm^2 s^{-1}], and v is the potential scan rate in [V s^{-1}]. D was taken from the literature and equal to 6.2×10^{-6} cm^2 s^{-1} in 0.1 M KCl [54].

The transfer coefficient (α) was obtained from the anodic region of the Tafel slope and shown in Table 4 as referenced in [53]. The coefficient α decreased from 0.421 to 0.371 with an increase in the potential scan rate, with an average value of 0.392 for LINDCN_CO_2-1. For LINDCN_CO_2-2, the α values exhibited a similar trend, decreasing from 0.547 to 0.410 (from 25 to 200 mV s^{-1}) with an average value of 0.455. This is closer to the ideal value of 0.5 [53] than for LINDCN_CO_2-1. This fact again shows that the CO_2 laser parameters need further optimization to achieve reproducible electrochemical properties.

The electroactive area was calculated using Equation (2) with the average value of α inserted. The data are shown in Table 4. LINDCN_CO_2-2 had a larger electroactive area (A_{EA}) than LINDCN_CO_2-1, 0.187 and 0.035 cm^3, respectively. However, in both cases, this was significantly smaller than the geometric area of the electrodes (1 cm^3). Again, it confirms that these electrodes have limited application for electrochemical sensing without further modification or optimization of the laser parameters.

LINDCN_532 electrodes had significantly different CV profiles under the same electrochemical conditions (Figure 5C,D). The current density was at least 10 times higher than at LINDCN_CO_2 electrodes, and the peak separation increased significantly with the increase in the potential scan rate. The ΔE_p increased from 200 to almost 500 mV (depending on the electrode), which is likely an irreversible electrochemical reaction. However, the I_{ox}/I_{red} ratio was closer to reversible/quasi-reversible reactions, i.e., 1.09 and 1.06 for LINDCN_532-1 and LINDCN_532-2, respectively. This indicates the potential drop across the electrical double layer and/or the potential drop across the bulk electrolyte of the electrodes due to surface porosity; therefore, the ohmic compensation is required [55,56]. To apply the *IR* compensation, EIS spectra were analyzed, and cell resistance was used for the ohmic drop compensation. The CVs after this correction showed reversible to quasi-reversible behavior with ΔE_p from 59 to 135 mV, depending on the potential scan rate (Table 4).

The α values were obtained from Tafel plots and were dependent on the potential scan rate. The data are provided in Table 4. Interestingly, the α values were lower for the LINDCN_532 electrodes than for the LINDCN_CO_2 electrodes. Similar α values of 0.3 were obtained for unmodified screen-printed graphite electrodes, since usually α for quasi-reversible reactions is between 0.3 and 0.5. The obtained α values were used to

calculate the A_{EA}; the data are given in Table 4. The A_{EA} was 3.43 cm^3 and 4.07 cm^3 for LINDCN_532-1 and LINDCN_532-2, respectively, which is much higher than the geometric area (1 cm^3). These results confirm that the porosity of the LINDCN_532 electrodes, as seen in the SEM images (Figure 1E–H), contributes to the large electroactive area. These electrodes can be suitable for use in electrochemical sensing, since the large electroactive area improves sensitivity.

Table 4. Parameters of CV analysis for LINDCN electrodes. Data are given after ohmic compensation.

Electrode	v, V s^{-1}	I_{ox}/I_{red}	ΔE, mV	α	k_0, cm s^{-1}	A_{EA}, cm^2
LINDCN_CO_2-1	0.025	1.12	85	0.422		
	0.050	1.21	90	0.418		
	0.075	1.08	103	0.400		
	0.100	1.06	111	0.390		
	0.125	1.06	125	0.388		
	0.150	1.04	139	0.382		
	0.175	1.14	153	0.376		
	0.200	1.06	163	0.373		
Average		1.10	121 ± 36	0.394 ± 0.021	0.487 ± 0.022	0.035 ± 0.003
LINDCN_CO_2-2	0.025	1.132	78	0.573		
	0.050	1.005	85	0.494		
	0.075	0.944	95	0.472		
	0.100	0.903	101	0.440		
	0.125	0.836	114	0.438		
	0.150	0.798	126	0.433		
	0.175	0.797	130	0.427		
	0.200	0.785	137	0.420		
Average		0.900	108 ± 30	0.462 ± 0.042	0.651 ± 0.009	0.166 ± 0.028
LINDCN_532-1	0.025	1.073	59	0.313		
	0.050	1.058	65	0.290		
	0.075	1.072	70	0.269		
	0.100	1.112	90	0.274		
	0.125	1.111	90	0.267		
	0.150	1.085	110	0.264		
	0.175	1.066	120	0.253		
	0.200	1.121	125	0.255		
Average		1.087	92 ± 27	0.271 ± 0.016	2.25 ± 0.09	3.43 ± 0.15
LINDCN_532-2	0.025	1.007	59	0.309		
	0.050	1.027	60	0.287		
	0.075	1.046	65	0.268		
	0.100	1.081	85	0.249		
	0.125	1.097	100	0.251		
	0.150	1.099	110	0.254		
	0.175	1.075	115	0.250		
	0.200	1.045	135	0.247		
Average		1.060	91 ± 31	0.264 ± 0.017	5.66 ± 1.01	4.07 ± 0.12

Another parameter that describes electrode kinetics is the heterogeneous rate constant (k_0). However, there are many discussions about which model is more suitable for quasi-reversible and irreversible systems. Masood et al. [53] compared several methods for detecting k_0 in quasi-reversible electrochemical reactions. The authors found that the Kochi and Gileadi methods provided reliable k_0 values, whereas Nicholson and Shain's equation gave overestimated values. Nevertheless, they found that k_0 calculated from the plot of $v^{-1/2}$ versus Ψ, as derived from the Nicholson and Shain equation, agreed

well with values obtained using the Kochi and Gilaedi methods. It should be noted that their research aimed to calculate the *D* of paracetamol. Meanwhile, Guermeche et al. [57] compared k_0 when applying various equations to the electrochemical reaction in the hexacyanoferrate system. Argwal [58] conducted a thorough analysis of Nicholson's method, providing corrected Ψ values for determining k_0. We used the *D* value from the literature (as described above) to calculate k_0. The Ψ values were taken from this reference for further CV analysis. The k_0 values obtained around 0.5 cm s^{-1} again confirmed that, in the case of LINDCN_CO_2, electrons are transferred slowly at the electrode interface, thus confirming a quasi-reversible electrochemical reaction [57,58]. Furthermore, k_0 was found to be 2.25 and 5.66 cm s^{-1} for LINDCN_532-1 and LINDCN_532-2, respectively, indicating fast electrochemical reactions. However, the reproducibility of electron transfer at different samples from the same production batch was rather low, as was also evident from the EDS data (Table 1). This suggests that further optimization of the laser parameters for electrode fabrication on the PEI surface is required.

EIS is a powerful tool, which allows for assessing differences between electrode structures that it is not possible by voltammetric techniques such as CV or pulse voltammetries [59]. A comprehensive interpretation of impedance spectra in carbon-electrode-based systems often depends on having a predefined or well-organized molecular arrangement at the electrode or modified surface, ensuring uniformity at the nanoscale [60,61].

To evaluate the processes occurring at the solution–electrode interface, EIS was recorded at OCP in blank electrolyte (0.1 M KCl). The data are depicted in Figure 6A. The spectra have a small, misshaped semicircle (visible in the inset of Figure 6A) typical of carbon nanomaterials in buffer solution without a redox probe [62,63]. The classical or modified Randles equivalent circuit was not suitable for the fitting of an entire spectrum, since no redox species were in the solution. The same circuit for all the electrodes (presented in Figure 6B) was applied for the analysis of the spectra: spectra were fitted to the modified Randles (CPE was used instead of a capacitor) with another $R\|$CPE connected in series (R_Ω–[$R_{ct}\|$CPE$_{dl}$]–[$R_{LINDCN}\|$CPE$_{LINDCN}$]). The second couple $R\|$CPE is related to the electroactive species transfer through the LINDCD film.

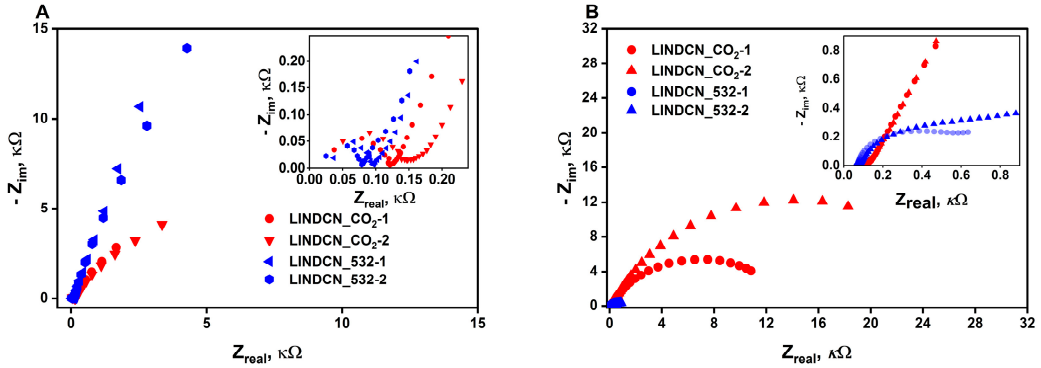

Figure 6. EIS spectra recorded at LINDCN_CO_2-1 (red circles), LINDCN_CO_2-2 (red triangles), LINDCN_532-1 (blue circles), and LINDCN_532-2 (blue triangles) in 0.1 M KCl (**A**) and in the presence of $[Fe(CN)_6]^{3-/4-}$ redox probe (**B**). Insets show the high-frequency region.

All parameters of the spectra fitting are given in Table 5. The cell resistance, R_Ω, represents solution and bull resistances, combined in series $R_{ct}\|$CPE$_{dl}$ (Figure 6B). R_{ct} is the charge-transfer resistance. CPE was modeled as a non-ideal capacitor [59]:

$$CPE = \frac{1}{C(i\omega)^{\alpha}} \quad (3)$$

where the capacitance C describes the charge separation at the double layer interface and the α exponent is due to the heterogeneity of the surface; when $\alpha = 1$, it is for a uniformly flat surface.

Table 5. Parameters obtained by analyzing EIS spectra in Figure 6A, in blank electrolyte and in 5.0 mM $[Fe(CN)_6]^{3-/4-}$ (Figure 6B). The equivalent circuits are described in the text. The fitting error (χ^3) was below 5% for all samples. C was calculated from CPE using the Brug relation (Equation (4)).

Electrode	R_Ω, Ω cm^2	C_{dl}, μF cm^{-2}	α_1	R_{ct}, kΩ cm^2	R_{LINDCN}, Ω cm^2	C_{LINDCN}, μF cm^{-2}	α_2
Blank electrolyte							
LINDCN_CO_2-1	114	62.4	0.812	15.2	17.3	42.2	0.761
LINDCN_CO_2-2	144	30.5	0.787	14.7	28.7	39.1	0.794
LINDCN_532-1	94.0	19.2	0.872	94.0	29.0	39.4	0.876
LINDCN_532-2	79.7	13.4	0.881	120	39.6	43.3	0.899
$[Fe(CN)_6]^{3-/4-}$							
LINDCN_CO_2-1	110	0.106	0.760	15.9			
LINDCN_CO_2-2	111	0.050	0.762	41.7			
LINDCN_532-1	75.6	258	0.746	0.794			
LINDCN_532-2	65.1	377	0.870	0.525			

According to the heterogeneity constant, the surface is more homogeneous at LINDCN_532 than at LINDCN_CO_2, which is consistent with the SEM data. The R_{ct} values at LINDCN_532 are almost ten times higher than at LINDCN_CO_2 at low frequencies and, because charge separation is predominant, as seen in the spectra, they have much higher imaginary impedance values (Figure 6A).

The redox probe helps to assess charge transfer at the interface; therefore, EIS spectra were recorded in the presence of the $[Fe(CN)_6]^{3-/4-}$. The obtained spectra are presented in Figure 6A, and they show clear semicircles typical of the behaviors where charge transfer is predominant. However, the semicircles are misshaped and have "tails" in the low-frequency region, indicating that diffusion is also important in the control of the electrochemical process [59]. The spectra were analyzed by non-linear least-squares fitting using equivalent circuit models. For LINDCN_532 electrodes, the spectra were fitted with the modified Randles circuit R_Ω–[(R_{ct} + W)‖CPE], and W is a semi-infinite Warburg element accounting for diffusion of redox species at low frequencies. The Warburg component was included due to the presence of a diffusion-controlled contribution observed in the low-frequency region.

In contrast, spectra obtained from CO_2 laser-fabricated electrodes exhibited no well-defined diffusion-controlled region within the investigated frequency window and were therefore fitted using a simplified Randles-type circuit R_Ω–(R_{ct}‖CPE), without inclusion of a Warburg element. The impedance values of the spectra show more difficult charge transfer, as the impedance values are higher than at LINDCN_532 electrodes. This is in good agreement with the characterization by CV. In all cases, the CPE accounts for surface heterogeneity and distributed interfacial time constants.

The effective double-layer capacitance (C_{dl}) was calculated from the fitted CPE parameters using the Brug relation [59]:

$$C_{dl} = \left(CPE \cdot R_{ct}^{1-n}\right)^{1/n} \quad (4)$$

and normalized to the geometric electrode area (1 cm^3). Only fits yielding low χ^3 values and physically meaningful parameters were considered acceptable.

The definition of the Warburg element used is [59]

$$Z_W(\omega) = R_{\text{dif}} \frac{\coth[(iT\omega)^{\alpha}]}{(iT\omega)^{\alpha}} \quad (5)$$

where R_{dif} is the diffusion resistance of electroactive species, t is the time constant depending on the diffusion rate ($t = l^2/D$, where l is the effective diffusion thickness and D is the effective diffusion coefficient of the species), and $\alpha = 0.5$ means a perfect uniformly flat interface. At high frequencies, the impedance behavior is that of infinite diffusion (phase angle 45°), and at low frequencies, it tends to that of a capacitor (phase angle 90°). Values of α of less than 0.5 express the fact that the interface is not uniform.

The EIS results recorded in the presence of the $[Fe(CN)_6]^{3-/4-}$ redox probe (Figure 6B, Table 5) provide direct insight into the interfacial charge-transfer properties of the LINDCN electrodes and strongly corroborate the trends observed in Raman, XPS, and CV analyses.

As shown in the Nyquist plots, the LINDCN_532 electrodes exhibit a dramatically reduced semicircle diameter compared to the LINDCN_CO_2 samples, indicating significantly faster electron-transfer kinetics. This is quantitatively reflected in the R_{ct}, which decreases from 15.9–41.7 kΩ·cm^3 for LINDCN_CO_2 to 0.525–0.794 kΩ·cm^3 for LINDCN_532. Such a reduction of nearly two orders of magnitude confirms that the electron-transfer process is severely hindered in LINDCN_CO_2 electrodes but highly efficient in the LINDCN_532 samples.

The discrepancies of R_{ct} in blank electrolyte and presence of the redox probe are caused by different processes dominating under different conditions. The blank electrolyte exhibits predominantly capacitive behavior, which reflects interfacial phenomena associated with the Helmholtz double layer and is governed mainly by mass transport rather than charge-transfer processes. In contrast, the addition of a redox probe enables the assessment of charge-transfer properties.

This behavior is directly consistent with the structural characterization. Raman analysis showed that LINDCN_532 exhibits larger in-plane crystallite sizes (L_a up to 8.0 nm) and lower disorder (lower FWHM(G) and $I_{D''}/I_G$), while XPS revealed a significantly higher sp^3 carbon fraction (≈55–59%) and the presence of π–π* shake-up satellites, indicative of extended aromatic domains. These features facilitate electron delocalization and reduce the energetic barrier for charge transfer, explaining the low R_{ct} values. In contrast, the LINDCN_CO_2 electrodes, characterized by high sp^3 content and abundant oxygen/nitrogen functional groups, exhibit disrupted electronic pathways and consequently sluggish charge-transfer kinetics.

The C_{dl} further supports this interpretation. The LINDCN_532 electrodes show exceptionally high capacitance values (258–377 μF·cm^{-3}), several orders of magnitude larger than those of the LINDCN_CO_2 electrodes (0.0499–0.106 μF·cm^{-3}). This increase reflects a significantly larger electrochemically active surface area, in agreement with CV-derived A_{EA} values (up to 4.07 cm^3) and SEM observations of finer, more accessible porous structures. The high capacitance indicates enhanced charge storage capability and improved electrode/electrolyte interaction.

The CPE exponent α provides additional insight into surface homogeneity. While CO_2-derived electrodes exhibit $\alpha \approx 0.76$, indicative of highly heterogeneous and defect-rich interfaces, LINDCN_532-2 shows a higher α value (0.87), suggesting a more uniform and ideal capacitive behavior. This again aligns with the improved structural ordering observed in Raman and XPS analyses.

Additionally, the lower solution resistance (R_Ω) observed for the LINDCN_532 electrodes (65–76 Ω·cm^3 vs. ~110 Ω·cm^3 for CO_2 samples) indicates improved overall conductivity and better electrical connectivity within the electrode structure.

Importantly, these EIS findings are fully consistent with the CV results. The LINDCN_532 electrodes exhibited significantly higher current densities, reversible behavior after ohmic correction, and higher heterogeneous rate constants (k_0 up to 5.66 cm·s^{-1}), whereas the LINDCN_CO_2 electrodes showed quasi-reversible behavior and much slower kinetics. Together, these results demonstrate that graphitic ordering and electronic transport properties dominate electrochemical performance, outweighing the potential benefits of higher surface functionalization.

A higher amount of defects usually improves the electrochemical properties of carbon nanomaterials, and a higher content of N and defects was found in LINDCN_CO_2 electrodes, but as seen from electrochemical characterization, its electrochemical performance was worse than at LINDCN_532. This apparent contradiction arises from the well-known trade-off between surface chemical activity and long-range electronic transport in carbon-based materials [64]. Specifically, an excessive number of defects can disrupt the percolating sp^3 network, leading to increased R_{ct} and thus poorer electrochemical performance [65].

Moreover, literature data confirm that a moderate nitrogen content enhances the electrochemical response, whereas excessive nitrogen incorporation leads to its deterioration [66]. The optimal nitrogen content reported in bulk graphene materials is approximately 6%, although this value may differ for LIG, as suggested by our results.

Overall, the EIS analysis confirms that LINDCN_532 carbon materials have superior interfacial charge-transfer properties, driven by enhanced graphitic structure, improved electronic conductivity, and increased electroactive surface area.

3.2. Detection of the Trace of Heavy Metals

The superior analytical performance of LINDCN_532 electrodes in heavy metal detection is directly correlated with their enhanced graphitic character and improved electron-transfer kinetics. XPS and Raman analyses revealed a significantly higher sp^3 carbon fraction, larger in-plane crystallite size (L_a up to 8.0 nm), and the presence of π–π* shake-up satellites, all indicative of extended aromatic domains and improved electronic delocalization. These structural characteristics translate into a dramatically reduced charge-transfer resistance ($R_{ct} \approx 0.66$ kΩ compared to 28.8 kΩ for CO_2-derived electrodes) and a substantially larger electroactive surface area (up to 4.07 cm^3). In contrast, although CO_2-treated samples exhibit higher nitrogen and oxygen functionalization, the predominance of sp^3 carbon and structural disorder limits electronic conductivity and results in sluggish electron-transfer kinetics, ultimately suppressing stripping current responses. Collectively, these findings demonstrate that, for electrochemical heavy metal sensing, efficient electronic transport and accessible electroactive surface area outweigh the benefits of increased heteroatom functionalization.

This structure–function relationship is clearly reflected in the analytical performance for individual metals. For Zn^{3+} detection (Figure 7B), LINDCN_532 exhibited a sensitivity approximately 2.7-fold higher than LINDCN_CO_2 (0.322 vs. 0.121 μA μM^{-1} cm^{-2}; normalized to geometric area), together with improved linearity (R^3 = 0.963 vs. 0.866) and lower relative slope uncertainty. The inferior response of the LINDCN_CO_2 electrodes is consistent with their higher charge-transfer resistance and smaller electroactive area, confirming that graphitic ordering and enhanced conductivity dominate stripping-based Zn^{3+} detection.

For Cd^{3+}, the difference between the two fabrication routes becomes even more pronounced. While LINDCN_532 provided a monotonic increase in stripping current with concentration, the LINDCN_CO_2 electrodes exhibited progressive peak broadening accompanied by a decrease in peak current (Figure 7C). At higher concentrations, the Cd stripping peak became indistinguishable from the background, preventing reliable

quantification across the tested range. This behavior suggests a transition to a surface-limited regime, likely driven by passivation and/or highly heterogeneous metal deposition on the defect-rich, poorly conductive CO_2-derived carbon surface. The sensitivity was 0.515 vs. −0.248 µA µM^{-1} cm^{-2} for LINDCN_532 and LINDCN_CO_2, respectively.

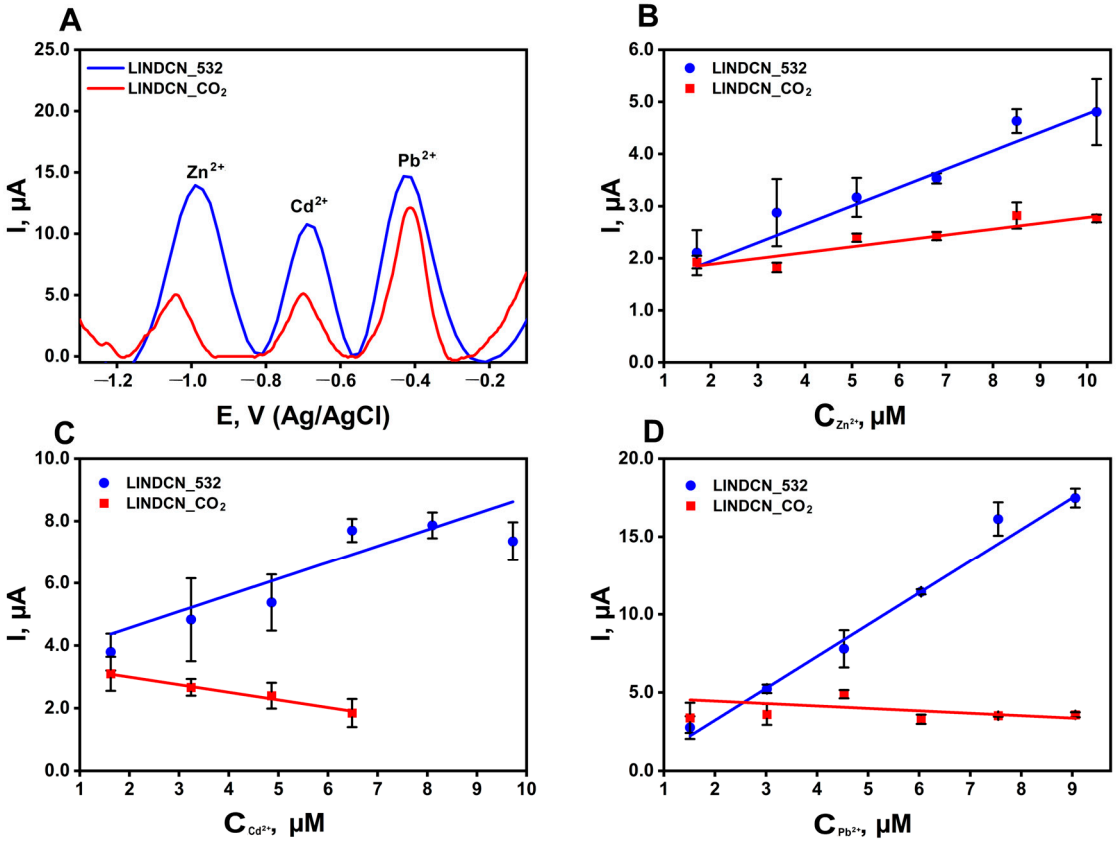

Figure 7. Representative stripping voltammograms showing peak currents (I_p) for Zn^{3+}, Cd^{3+}, and Pb^{3+} at ~6.8 µM obtained using LINDCN_CO_2 (red) and LINDCN_532 (blue) electrodes (**A**). Calibration curve for Zn^{3+} (**B**), Cd^{3+} (**C**) and Pb^{3+} (**D**). Error bars represent the standard deviation of replicate measurements (n = 3).

The contrast is most striking for Pb^{3+} detection (Figure 7D). LINDCN_532 demonstrated excellent analytical performance, with high sensitivity (2.04 ± 0.15 µA µM^{-1} cm^{-2}) and strong linear correlation (R^3 = 0.978), indicative of efficient nucleation and rapid stripping kinetics on the graphitized carbon framework. In contrast, LINDCN_CO_2 showed no statistically meaningful dependence of current on Pb^{3+} concentration ($R^3 \approx 0.006$), indicating that the defect-rich, high-resistance carbon structure is unsuitable for reliable Pb^{3+} quantification.

Such a signal decrease could be related to a specific binding of Pb^{3+} to the electrode surface. Since the detection is performed simultaneously, the preconcentration potential was set to the same value for all metals. LINDCN_CO_2 contains a higher amount of nitrogen than LINDCN_532, and it is well known that heavy metal ions can be coordinated by nitrogen-containing groups. Jin et al. [67] used density functional theory (DFT) to investigate the adsorption of various heavy metals on graphene and N-doped graphene surfaces. The authors found that N-doped graphene adsorbs transition metals with higher adsorption energies than pristine graphene and that these metals tend to form clusters on the surface. The geometry and size of these clusters depend on the nature of the metal: 4d and 5d metals exhibit different structures compared to 3d metals. Although the metals studied in our work were not included in the study by Jin et al., a similar trend can be

considered. Zinc is a 3d metal, whereas cadmium and lead (although the latter is not a transition metal) belong to the 4d and 5d groups, respectively. Based on this DFT study, we propose the hypothesis that Cd and Pb are more strongly adsorbed on LINDCN than Zn. On the other hand, LINDCN_532 contains a lower amount of nitrogen, which may lead to weaker adsorption of the metal analytes. As a result, these electrodes exhibit improved SWASV performance compared to LINDCN_CO_2 samples. The analytical parameters are summarized in Table 6. Sensitivity is normalized to the geometric electrode area because the electroactive area is a relative parameter that depends on the $[Fe(CN)_6]^{3-}/^{4-}$ redox probe and its electrochemical behavior. The redox couple is diffusion-controlled, whereas metal ions are preconcentrated through adsorption onto the electrode surface.

Table 6. Calibration parameters for Zn^{3+}, Cd^{3+}, and Pb^{3+} detection at LINDCN electrodes fabricated with 532 nm and CO_2 lasers, including sensitivity (slope), intercept, R^3, and relative error. NQ = not quantifiable.

Analyte	Electrode	Sensitivity *, μA μM^{-1} cm^{-2}	Intercept, μA cm^{-2}	R^3	Relative Error, %
Zn^{3+}	LINDCN_532	0.322 ± 0.031	1.606 ± 0.207	0.963	9.7
Zn^{3+}	LINDCN_CO_2	0.121 ± 0.024	1.639 ± 0.158	0.866	19.7
Cd^{3+}	LINDCN_532	0.515 ± 0.116	3.229 ± 0.733	0.831	22.6
Cd^{3+}	LINDCN_CO_2 **	0.248 ± 0.023	3.506 ± 0.100	0.984	9.1
Pb^{3+}	LINDCN_532	2.042 ± 0.154	−0.440 ± 0.907	0.978	7.6
Pb^{3+}	LINDCN_CO_2 ***	NQ	—	0.006	—

* Sensitivity is normalized to geometric area. ** Cd peak broadened and disappeared at higher concentrations; regression reflects a limited monotonic region only. *** No meaningful correlation between Pb^{3+} concentration and stripping current ($R^3 \approx 0.006$); electrode unsuitable for quantitative detection under tested conditions.

In the literature, LIG has been explored only rarely for the detection of heavy metals, and none of the reported studies specifically targeted Zn^{3+} detection. In most cases, modified or doped LIG electrodes were used. For example, Jeong et al. [68] reported Ag-nanoparticle-incorporated LIG electrodes for the detection of Cd^{3+}, Pb^{3+}, and Cu^{3+}. The reported sensitivities were 0.271 and 0.037 μA μM^{-1} cm^{-2} for Cd^{3+} and Pb^{3+}, respectively, in model solutions, and 0.034 and 0.025 μA nM^{-1} in tap water. Chaudhary et al. [69] used N- and B-co-doped LIG electrodes to detect Cd^{3+} and Pb^{3+}, achieving sensitivities of 0.661 and 0.725 μA μM^{-1}, respectively. Chu et al. [70] employed Bi film modified LIG to detect Cd^{3+} and Pb^{3+}, with sensitivities of 0.000410 and 0.000792 μA μM^{-1}, respectively. In this context, LINDCN electrodes exhibit comparable sensitivity, although in some cases the reported sensitivities appear to be much lower, which is likely because they are not normalized to the electrode area, as the authors do not specify the geometric area of the electrodes. Importantly, LINDCN electrodes enable the detection of Zn^{3+}.

Overall, these results consistently demonstrate that electron-transfer efficiency and effective electroactive surface accessibility govern analytical performance more strongly than surface functional group density. The different laser processing, therefore, critically determines the balance between structural order and defect density, which in turn defines the suitability of laser-induced carbon nanomaterials as platforms for electrochemical heavy metal sensing.

4. Conclusions

This empirical study demonstrates that both CO_2 and 532 nm lasers are suitable for electrode fabrication on PEI substrates. By combining structural (SEM, Raman, XPS) and electrochemical (CV, EIS) analyses, relationships between graphitic ordering and interfacial charge-transfer behavior were identified under the investigated processing conditions.

Under the selected fabrication parameters, the LINDCN_532 samples exhibited a higher apparent degree of graphitization, characterized by increased sp^3 carbon content, larger in-plane crystallite size, and extended aromatic domains. These features were associated with lower charge-transfer resistance, larger electroactive surface area, and faster electron-transfer kinetics.

In contrast, LINDCN_CO_2 samples displayed a higher degree of surface functionalization but also greater structural disorder, which correlated with reduced conductivity and less favorable electrochemical performance under the same conditions.

These differences were reflected in analytical applications, where the LINDCN_532 electrodes showed improved sensitivity, linearity, and quantification performance for Zn^{3+}, Cd^{3+}, and Pb^{3+} detection within the tested parameter space.

Importantly, these results should not be interpreted as a direct comparison of fully optimized fabrication regimes but rather as an indication of how different laser–material interaction modes can influence the resulting structure and electrochemical behavior.

More broadly, the findings suggest that irradiation parameters must be carefully tailored to balance structural order and surface chemistry depending on the target application. Defect-rich, functionalized materials may be advantageous for catalytic or adsorption-driven processes, whereas more graphitized structures may benefit sensing platforms requiring efficient electron transfer.

Future work will focus on systematic optimization of processing parameters for each laser system and on establishing causal structure–property relationships through controlled parameter variation. In addition, hybrid strategies combining graphitic backbones with controlled surface functionalization or nanomaterial integration will be explored.

Overall, this work provides a foundation for the rational engineering of laser-induced carbon materials and highlights the importance of processing conditions in tuning electrochemical performance.

Author Contributions: Conceptualization, P.R.R., J.G. and R.P.; methodology, P.R.R., A.S., T.M., S.S. and R.T.; software, R.P., A.S., T.M. and J.G.; validation, P.R.R.; formal analysis, P.R.R., Š.M., A.S., T.M., S.S., R.T., J.G. and R.P.; investigation, R.P., Š.M., A.S., T.M. and S.S.; resources, R.P.; data curation, P.R.R.; writing—original draft preparation, P.R.R., T.M., J.G. and R.P.; writing—review and editing, R.P., A.S., T.M., S.S., R.T., J.G. and R.P.; visualization, P.R.R., A.S., T.M., S.S., R.T. and J.G.; supervision, R.T. and R.P. All authors have read and agreed to the published version of the manuscript.

Funding: This research received no external funding.

Data Availability Statement: The original contributions presented in this study are included in the article. Further inquiries can be directed to the corresponding author.

Conflicts of Interest: The authors declare no conflicts of interest.

References

1. Ramezani, M.J.; Rahmani, O. A Review of Recent Progress in the Graphene Syntheses and Its Applications. *Mechan. Adv. Mater. Struct.* **2025**, *32*, 5256–5288. [CrossRef]
2. Avinash, K.; Patolsky, F. Laser-Induced Graphene Structures: From Synthesis and Applications to Future Prospects. *Mater. Today* **2023**, *70*, 104–136. [CrossRef]
3. Liu, M.; Wu, J.; Cheng, H. Effects of Laser Processing Parameters on Properties of Laser-Induced Graphene by Irradiating CO_2 Laser on Polyimide. *Sci. China Technol. Sci.* **2022**, *65*, 41–52. [CrossRef]
4. Hristovski, I.R.; Herman, L.A.; Mitchell, M.E.; Lesack, N.I.; Reich, J.; Holzman, J.F. Manifestations of Laser-Induced Graphene under Ultraviolet Irradiation of Polyimide with Varied Optical Fluence. *Nanomaterials* **2022**, *12*, 1241. [CrossRef] [PubMed]
5. Dwivedi, T.; Padma Nilaya, J.; Kedia, S.; Das, R.C. Parametric Analysis of CW CO_2 Laser-Induced Graphene on Polyimide. *J. Vac. Sci. Technol. B* **2025**, *43*, 062804. [CrossRef]
6. Liu, H.; Chen, K.; Wu, R.; Pan, S.; Zhang, C. Laser-Induced Graphene-Based Flexible Substrate with Photothermal Conversion and Photoresponse Performance on Polyimide Film. *ACS Appl. Mater. Interfaces* **2023**, *15*, 46550–46558. [CrossRef] [PubMed]

7. Xu, X.; Cao, D.; Wei, Y.; Wang, A.; Chen, G.; Wang, T.; Wang, G.; Chen, X. Impact of Graphitization Degree on the Electrochemical and Thermal Properties of Coal. *ACS Omega* **2024**, *9*, 2443–2456. [CrossRef]
8. Wrogemann, J.M.; Fromm, O.; Deckwirth, F.; Beltrop, K.; Heckmann, A.; Winter, M.; Placke, T. Impact of Degree of Graphitization, Surface Properties and Particle Size Distribution on Electrochemical Performance of Carbon Anodes for Potassium-Ion Batteries. *Batter. Supercaps* **2022**, *5*, e202200045. [CrossRef]
9. Goldie, S.J.; Bush, S.; Cumming, J.A.; Coleman, K.S. A Statistical Approach to Raman Analysis of Graphene-Related Materials: Implications for Quality Control. *ACS Appl. Nano Mater.* **2020**, *3*, 11229–11239. [CrossRef]
10. Nanda, S.S.; Kim, M.J.; Yeom, K.S.; An, S.S.A.; Ju, H.; Yi, D.K. Raman Spectrum of Graphene with Its Versatile Future Perspectives. *TrAC Trends Anal. Chem.* **2016**, *80*, 125–131. [CrossRef]
11. Moseenkov, S.I.; Kuznetsov, V.L.; Zolotarev, N.A.; Kolesov, B.A.; Prosvirin, I.P.; Ishchenko, A.V.; Zavorin, A.V. Investigation of Amorphous Carbon in Nanostructured Carbon Materials (A Comparative Study by TEM, XPS, Raman Spectroscopy and XRD). *Materials* **2023**, *16*, 1112. [CrossRef]
12. Panigrahi, K.; Mal, S.; Bhattacharyya, S. Deciphering Interfacial Charge Transfer Mechanisms in Electrochemical Energy Systems through Impedance Spectroscopy. *J. Mater. Chem. A* **2024**, *12*, 14334–14353. [CrossRef]
13. Vivier, V.; Orazem, M.E. Impedance Analysis of Electrochemical Systems. *Chem. Rev.* **2022**, *122*, 11131–11168. [CrossRef] [PubMed]
14. Zhang, Z.; Zhu, H.; Zhang, W.; Zhang, Z.; Lu, J.; Xu, K.; Liu, Y.; Saetang, V. A Review of Laser-Induced Graphene: From Experimental and Theoretical Fabrication Processes to Emerging Applications. *Carbon* **2023**, *214*, 118356. [CrossRef]
15. Abdulhafez, M.; Tomaraei, G.N.; Bedewy, M. Fluence-Dependent Morphological Transitions in Laser-Induced Graphene Electrodes on Polyimide Substrates for Flexible Devices. *ACS Appl. Nano Mater.* **2021**, *4*, 2973–2986. [CrossRef]
16. Vander Wal, R.; Sengupta, A.; Musselman, E.; Skoptsov, G. Microwave-Driven Plasma-Mediated Methane Cracking: Product Carbon Characterization. *J. Carbon Res.* **2018**, *4*, 61. [CrossRef]
17. Wu, Z.; Sahaluddin, M.; Mustafa, D.B.; Ghosha, S.; Bedewy, M. Laser-induced graphene: From precursor chemistry to process control and throughput–resolution–performance trade-offs. *Nanoscale* **2026**, *18*, 6647. [CrossRef]
18. Fiodorov, V.; Trusovas, R.; Mockus, Z.; Ratautas, K.; Račiukaitis, G. Laser-induced graphene formation on polyimide using UV to mid-infrared laser radiation. *Polymers* **2023**, *15*, 4229. [CrossRef]
19. Moussa, S.; Atkinson, G.; SamyEl-Shall, M.; Shehata, A.; AbouZeid, K.M.; Mohamed, M.B. Laser assisted photocatalytic reduction of metal ions by graphene oxide. *J. Mater. Chem.* **2011**, *21*, 9608–9619. [CrossRef]
20. Altuwirqi, R.M. Graphene nanostructures by pulsed laser ablation in liquids: A review. *Materials* **2022**, *15*, 5925. [CrossRef]
21. Ye, R.; James, D.K.; Tour, J.M. Laser-induced graphene: From discovery to translation. *Adv. Mater.* **2019**, *31*, 1803621. [CrossRef]
22. Botti, S.; Bonfigli, F.; Bruttomesso, A.; Micciulla, F.; Nigro, V.; Rufoloni, A.; Vannozzi, A. CO_2 and UV laser-induced graphene based on polymer transformation: Advanced characterizations by 2D rama mapping combined with microscopy techniques. *Materials* **2025**, *18*, 3119. [CrossRef]
23. Fatkullin, M.; Cheshev, D.; Averkiev, A.; Gorbunova, A.; Murastov, G.; Liu, J.; Postnikov, P.; Cheng, C.; Rodriguez, E.D.; Sheremet, E. Photochemistry dominates over photothermal effects in the laser-induced reduction of graphene oxide by visible light. *Nat. Commun.* **2024**, *15*, 9711. [CrossRef] [PubMed]
24. Chemello, G.; Radnik, J.; Hodoroaba, V.D. XPS–SEM/EDS tandem analysis for the elemental composition of functionalized graphene nanoplatelets. *ACS Omega* **2025**, *45*, 54601–54607. [CrossRef]
25. Krishna, D.N.G.; Philip, J. Review on surface-characterization applications of X-ray photoelectron spectroscopy (XPS): Recent developments and challenges. *Appl. Surf. Sci. Adv.* **2022**, *12*, 100332. [CrossRef]
26. Ma, C.; Kumagai, S.; Sato, M.; Nakai, Y.; Saito, Y.; Watanabe, A.; Watanabe, C.; Teramae, N.; Yoshioka, T. Investigating the degradation and products of thermo-oxidation of polyimide-based engineering plastics. *J. Anal. Appl. Pyrolysis* **2024**, *181*, 106575. [CrossRef]
27. Trusovas, R.; Ratautas, K.; Račiukaitis, G.; Niaura, G. Graphene Layer Formation in Pinewood by Nanosecond and Picosecond Laser Irradiation. *Appl. Surf. Sci.* **2019**, *471*, 154–161. [CrossRef]
28. Wang, L.; Wang, Z.; Bakhtiyari, A.N.; Zheng, H. A Comparative Study of Laser-Induced Graphene by CO_2 Infrared Laser and 355 Nm Ultraviolet (UV) Laser. *Micromachines* **2020**, *11*, 1094. [CrossRef]
29. Daffan, G.; Kothuru, A.; Eran, A.; Patolsky, F. In-Situ Laser Synthesis of Molecularly Dispersed and Covalently Bound Phosphorus-Graphene Adducts as Self-Standing 3D Anodes for High-Performance Fast-Charging Lithium-Ion Batteries. *Adv. Energy Mater.* **2024**, *14*, 2401832. [CrossRef]
30. Aukštakojytė, R.; Niaura, G.; Bukauskas, V.; Barkauskas, J.; Pauliukaitė, R.; Gaidukevič, J. Bismarck Brown-Assisted Hydrothermal Synthesis of Nitrogen-Modified Reduced Graphene Oxide for Selective Electrochemical Detection of Dopamine. *Surf. Interfaces* **2024**, *46*, 104041. [CrossRef]
31. Liu, K.; Song, S.; Sui, L.; Wu, S.; Jing, P.; Wang, R.; Li, Q.; Wu, G.; Zhang, Z.; Yuan, K.; et al. Efficient Red/Near-Infrared-Emissive Carbon Nanodots with Multiphoton Excited Upconversion Fluorescence. *Adv. Sci.* **2019**, *6*, 1900766. [CrossRef]

32. Chen, X.; Wang, X.; Fang, D. A Review on C1s XPS-Spectra for Some Kinds of Carbon Materials. *Fuller. Nanotub. Carbon Nanostruct.* **2020**, *28*, 1048–1058. [CrossRef]
33. Morimoto, N.; Kubo, T.; Nishina, Y. Tailoring the Oxygen Content of Graphite and Reduced Graphene Oxide for Specific Applications. *Sci. Rep.* **2016**, *6*, 21715. [CrossRef]
34. Jeong, H.S.; Kim, D.; Lee, G.H.; Zhang, L.; Kim, Y.; Lee, J.; Kim, M.K.; Kim, D.; Hong, J.P.; Park, W.B.; et al. Cross-Linked Amine Interface Engineering Strategy for High Performance Anode-Free Lithium-Metal Batteries with High-Loading Cathodes. *Adv. Funct. Mater.* **2025**, *36*, e27860. [CrossRef]
35. Snyder, R.L.; Lidston, C.A.L.; De Hoe, G.X.; Parvulescu, M.J.S.; Hillmyer, M.A.; Coates, G.W. Mechanically Robust and Reprocessable Imine Exchange Networks from Modular Polyester Pre-Polymers. *Polym. Chem.* **2020**, *11*, 5346–5355. [CrossRef]
36. Jorio, A.; Souza Filho, A.G. Raman Studies of Carbon Nanostructures. *Annu. Rev. Mater. Res.* **2016**, *46*, 357–382. [CrossRef]
37. Wu, J.-B.; Lin, M.-L.; Cong, X.; Liu, H.-N.; Tan, P.-H. Raman Spectroscopy of Graphene-Based Materials and Its Applications in Related Devices. *Chem. Soc. Rev.* **2018**, *47*, 1822–1873. [CrossRef]
38. Gaidukevič, J.; Trusovas, R.; Sartanavičius, A.; Pauliukaitė, R.; Niaura, G.; Kozłowski, M.; Barkauskas, J. Investigation of Picosecond Laser-Induced Graphene for Dopamine Sensing: Influence of Laser Wavelength on Structural and Electrochemical Performance. *Mater. Res. Bull.* **2024**, *178*, 112916. [CrossRef]
39. Trusovas, R.; Račiukaitis, G.; Niaura, G.; Barkauskas, J.; Valušis, G.; Pauliukaite, R. Recent Advances in Laser Utilization in the Chemical Modification of Graphene Oxide and Its Applications. *Adv. Opt. Mater.* **2016**, *4*, 37–65. [CrossRef]
40. Muzyka, K.; Xu, G. Laser-induced Graphene in Facts, Numbers, and Notes in View of Electroanalytical Applications: A Review. *Electroanalysis* **2022**, *34*, 574–589. [CrossRef]
41. Claramunt, S.; Varea, A.; López-Díaz, D.; Velázquez, M.M.; Cornet, A.; Cirera, A. The Importance of Interbands on the Interpretation of the Raman Spectrum of Graphene Oxide. *J. Phys. Chem. C* **2015**, *119*, 10123–10129. [CrossRef]
42. Le, G.T.T.; Manyam, J.; Opaprakasit, P.; Chanlek, N.; Grisdanurak, N.; Sreearunothai, P. Divergent Mechanisms for Thermal Reduction of Graphene Oxide and Their Highly Different Ion Affinities. *Diam. Relat. Mater.* **2018**, *89*, 246–256. [CrossRef]
43. Ferrari, A.C.; Robertson, J. Resonant Raman Spectroscopy of Disordered, Amorphous, and Diamondlike Carbon. *Phys. Rev. B* **2001**, *64*, 075414. [CrossRef]
44. Ribeiro-Soares, J.; Oliveros, M.E.; Garin, C.; David, M.V.; Martins, L.G.P.; Almeida, C.A.; Martins-Ferreira, E.H.; Takai, K.; Enoki, T.; Magalhães-Paniago, R.; et al. Structural Analysis of Polycrystalline Graphene Systems by Raman Spectroscopy. *Carbon* **2015**, *95*, 646–652. [CrossRef]
45. Rabti, A.; Baachaoui, S.; Zouari, M.; Raouafi, N. Laser-Induced Graphene Electrodes Obtained by Direct Laser Writing for Pharmaceutical and Biomedical Analysis. *J. Pharm. Biomed. Anal. Open* **2025**, *5*, 100069. [CrossRef]
46. Materón, E.M.; Azevedo, L.M.L.D.; Dias, J.M.; Pereira, K.C.R.; Sousa, G.M.; Dias, M.S.; Maroneze, C.M.; Dias, D.; Silva, C.D.C.C. Advancing Biomedical Analysis: Harnessing Laser-Induced Graphene for next-Gen of Low-Cost Sensor Technology. *J. Pharm. Biomed. Anal. Open* **2025**, *5*, 100077. [CrossRef]
47. Huang, L.; Liu, Y.; Ji, L.-C.; Xie, Y.-Q.; Wang, T.; Shi, W.-Z. Pulsed Laser Assisted Reduction of Graphene Oxide. *Carbon* **2011**, *49*, 2431–2436. [CrossRef]
48. Madito, M.J. Revisiting the Raman Disorder Band in Graphene-Based Materials: A Critical Review. *Vib. Spectrosc.* **2025**, *139*, 103814. [CrossRef]
49. Wan, Z.; Umer, M.; Lobino, M.; Thiel, D.; Nguyen, N.-T.; Trinchi, A.; Shiddiky, M.J.A.; Gao, Y.; Li, Q. Laser Induced Self-N-Doped Porous Graphene as an Electrochemical Biosensor for Femtomolar miRNA Detection. *Carbon* **2020**, *163*, 385–394. [CrossRef]
50. Cardoso, A.R.; Marques, A.C.; Santos, L.; Carvalho, A.F.; Costa, F.M.; Martins, R.; Sales, M.G.F.; Fortunato, E. Molecularly-Imprinted Chloramphenicol Sensor with Laser-Induced Graphene Electrodes. *Biosens. Bioelectron.* **2019**, *124–125*, 167–175. [CrossRef]
51. Soares, R.R.A.; Hjort, R.G.; Pola, C.C.; Parate, K.; Reis, E.L.; Soares, N.F.F.; McLamore, E.S.; Claussen, J.C.; Gomes, C.L. Laser-Induced Graphene Electrochemical Immunosensors for Rapid and Label-Free Monitoring of *Salmonella Enterica* in Chicken Broth. *ACS Sens.* **2020**, *5*, 1900–1911. [CrossRef]
52. Faulkner, L.L.; Bard, A.J. *Electrochemical Methods and Applications*, 2nd ed.; Wiley: New York, NY, USA, 2001; ISBN 978-0-471-04372-0.
53. Masood, Z.; Muhammad, H.; Tahiri, I.A. Comparison of Different Electrochemical Methodologies for Electrode Reactions: A Case Study of Paracetamol. *Electrochem* **2024**, *5*, 57–69. [CrossRef]
54. Pauliukaite, R.; Ghica, M.E.; Fatibello-Filho, O.; Brett, C.M.A. Comparative Study of Different Cross-Linking Agents for the Immobilization of Functionalized Carbon Nanotubes within a Chitosan Film Supported on a Graphite−Epoxy Composite Electrode. *Anal. Chem.* **2009**, *81*, 5364–5372. [CrossRef]
55. Son, Y.J.; Marquez, R.A.; Kawashima, K.; Smith, L.A.; Chukwuneke, C.E.; Babauta, J.; Mullins, C.B. Navigating *iR* Compensation: Practical Considerations for Accurate Study of Oxygen Evolution Catalytic Electrodes. *ACS Energy Lett.* **2023**, *8*, 4323–4329. [CrossRef]

56. Zheng, W. *iR* Compensation for Electrocatalysis Studies: Considerations and Recommendations. *ACS Energy Lett.* **2023**, *8*, 1952–1958. [CrossRef]
57. Saad Guermeche, R.; Affoune, A.M.; Houam, S.; Atek, I.; Vautrin-Ul, C.; Nacef, M.; Chelaghmia, M.L.; Girault, H.H.; Banks, C.E.; Djaghout, I. Computational and Experimental Determination of Electrochemical Standard Rate Constant from Cyclic Voltammetry: Insights into $\alpha + \beta \neq 1$ Systems. *RSC Adv.* **2025**, *15*, 50571–50581. [CrossRef]
58. Agarwal, R. The Nicholson Method of Determination of the Standard Rate Constant of a Quasireversible Redox Couple Employing Cyclic Voltammetry: Everything One Needs to Know! *ACS Electrochem.* **2025**, *1*, 1885–1894. [CrossRef]
59. Pauliukaite, R.; Ghica, M.E.; Fatibello-Filho, O.; Brett, C.M.A. Electrochemical Impedance Studies of Chitosan-Modified Electrodes for Application in Electrochemical Sensors and Biosensors. *Electrochim. Acta* **2010**, *55*, 6239–6247. [CrossRef]
60. Pianta, N.; Scarpioni, F.; Chukwu, R.; La Mantia, F.; Ruffo, R. Evaluation of Kinetic Parameters of Non-Faradic Processes in Carbon-Based Electrodes Using Multisine Dynamic Electrochemical Impedance Spectroscopy. *Electrochim. Acta* **2023**, *437*, 141462. [CrossRef]
61. Das, S.; Banerjee, A.; Nandi, U.; Ghosh, A. Critical Review on the Analysis of Electrochemical Impedance Spectroscopy Data. *J. Appl. Phys.* **2025**, *138*, 125002. [CrossRef]
62. Gong, Y.; Li, D.; Fu, Q.; Pan, C. Influence of Graphene Microstructures on Electrochemical Performance for Supercapacitors. *Prog. Nat. Sci. Mater. Internat.* **2015**, *25*, 379–385. [CrossRef]
63. Angizi, S.; Hong, L.; Huang, X.; Selvaganapathy, P.R.; Kruse, P. Graphene versus Concentrated Aqueous Electrolytes: The Role of the Electrochemical Double Layer in Determining the Screening Length of an Electrolyte. *npj 2D Mater. Appl.* **2023**, *7*, 67. [CrossRef]
64. Ambrosi, A.; Chua, C.K.; Latiff, N.M.; Loo, A.H.; Wong, C.H.A.; Eng, A.Y.S.; Bonannia, A.; Pumera, M. Graphene and its electrochemistry—An update. *Chem. Soc. Rev.* **2016**, *45*, 2458–2493. [CrossRef]
65. Tite, T.; Chiticaru, E.A.; Burns, J.S.; Ionita, M. Impact of nano-morphology, lattice defects and conductivity on the performance of graphene based electrochemical biosensors. *J. Nanobiotechnol.* **2019**, *17*, 101. [CrossRef]
66. Talukder, N.; Wang, Y.; Nunna, B.B.; Lee, E.S. Nitrogen-doped graphene nanomaterials for electrochemical catalysis/reactions: A review on chemical structures and stability. *Carbon* **2021**, *185*, 198–214. [CrossRef]
67. Jin, C.; Cheng, L.; Feng, G.; Ye, R.; Lu, Z.H.; Zhang, R.; Yu, X. Adsorption of Transition-Metal Clusters on Graphene and N-Doped Graphene: A DFT Study. *Langmuir* **2022**, *38*, 3694−3710. [CrossRef]
68. Jeong, S.; Yang, S.; Lee, Y.J.; Lee, S.H. Laser-induced graphene incorporated with silver nanoparticles applied for heavy metal multi-detection. *J. Mater. Chem. A* **2023**, *11*, 13409–13418. [CrossRef]
69. Chaudhary, Y.; Suman, S.; Rakesh, B.; Ojha, G.P.; Deshpande, U.; Pant, B.; Sankaran, K.J. Boron and nitrogen co-doped porous graphene nanostructures for the electrochemical detection of poisonous heavy metal ions. *Nanomaterials* **2024**, *14*, 806. [CrossRef] [PubMed]
70. Chu, G.; Zhang, Y.; Zhou, Z.; Zheng, W.; Chen, D.; Yu, S.; Wang, J.; Gui, Y.; Sun, X.; Li, M. Rapid CO_2-laser scribing fabrication of an electrochemical sensor for the direct detection of Pb^{2+} and Cd^{2+}. *Nano Res.* **2023**, *16*, 7671–7681. [CrossRef]